Weierstraß–Institut
für Angewandte Analysis und Stochastik

im Forschungsverbund Berlin e.V.

Technical Report ISSN 1618 – 7776

An Operator–Splitting Finite–Element Approach to an 8:1 Thermal Cavity Problem

Dominic Davis, Eberhard Bänsch

Weierstrass Institute for Applied Analysis and Stochastics

E-Mail: davis@wias-berlin.de baensch@wias-berlin.de

submitted: 15th November 2001

Technical Report No. 1
Berlin 2001

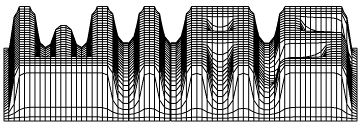

2000 *Mathematics Subject Classification.* 65N22, 65Y20,65N30, 65N50.

Key words and phrases. finite–element, advection, Navier–Stokes, CG method, GMRES, Galerkin.

Edited by
Weierstraß–Institut für Angewandte Analysis und Stochastik (WIAS)
Mohrenstraße 39
D — 10117 Berlin
Germany

Fax: + 49 30 2044975
E-Mail (X.400): c=de;a=d400-gw;p=WIAS-BERLIN;s=preprint
E-Mail (Internet): preprint@wias-berlin.de
World Wide Web: http://www.wias-berlin.de/

An Operator–Splitting Finite–Element Approach to an 8:1 Thermal Cavity Problem [1]

Dominic Davis, Eberhard Bänsch

Weierstrass Institute for Applied Analysis and Stochastics, Mohrenstrasse 39, 10117 Berlin, Germany

Abstract

This article describes the methodology for, and results obtained from, our contribution to a thermal-cavity benchmark test, described in [2]. Our solutions were obtained on graded rectangular grids for two different time-discretisation schemes by applying a finite-element procedure to the model equations, and a combination of conjugated-gradient (CG) and GMRES solvers to the resulting matrix systems.

Keywords: finite-element, advection, Navier–Stokes, CG method, GMRES, Galerkin

1 Introduction

Here we describe our contribution to a thermal-cavity benchmark problem held at the First MIT Conference on Computational Fluid and Solid Mechanics 2001. A full detailed account of the problem can be found in [2], but for the sake of self-containment we re-iterate the main details and motivation here. The chief aim of the benchmark test was to assess the reliability of computational predictions for the behaviour of a slightly supercritical flow in an air-filled (Prandtl number=0.71), differentially-heated, non-porous cavity of vertical aspect ratio 8, with adiabatic top and bottom walls. With the knowledge that the unstable eigenmode is unique within an approximate range of Rayleigh numbers $3.20 \times 10^5 - 3.50 \times 10^5$ [8], a Rayleigh number of 3.4×10^5 was selected. Furthermore, this mode is known *a priori* to possess the skew-symmetry property of the base flow. Several aspects make this seemingly "straightforward" problem surprisingly challenging: firstly, within a relatively small range of Rayleigh numbers ($3.06 \times 10^5 - 4.00 \times 10^5$) there exist four distinct unstable modes; although these do not *all* appear simultaneously for a given Rayleigh number in this range, multiple branches consisting of two or three of these occur for Rayleigh numbers in the ranges $3.06 \times 10^5 - 3.20 \times 10^5$ and $3.50 \times 10^5 - 4.00 \times 10^5$; secondly, the relatively large Rayleigh number produces small diffusion coefficients in both momentum and energy equations, making the simulation susceptible to numerical damping and/or dispersion either occurring naturally through inappropriate time discretisation methods for advection-dominated flows (such as

[1] based on a contribution to a benchmark test held at the First MIT Conference on Computational Fluid and Solid Mechanics 2001

first-order backward Euler), or else as a casualty of over-damping of spurious pressure modes (such as with upwinding).

The non-dimensional governing equations are the incompressible Navier–Stokes equations with Boussinesq approximation, the mass-conservation equation and the energy equation:

$$\frac{\partial \mathbf{u}}{\partial t} + (\mathbf{u} \cdot \nabla)\,\mathbf{u} - \sqrt{\frac{Pr}{Ra}}\Delta \mathbf{u} + \nabla p - T\hat{\mathbf{e}}_y = \mathbf{0} \quad \text{in } \Omega, \tag{1.1a}$$

$$\nabla \cdot \mathbf{u} = 0 \quad \text{in } \Omega; \tag{1.1b}$$

and

$$\frac{\partial T}{\partial t} + (\mathbf{u} \cdot \nabla)\,T - \frac{1}{\sqrt{RaPr}}\Delta T = 0 \quad \text{in } \Omega; \tag{1.1c}$$

where $\mathbf{u} = u\hat{\mathbf{e}}_x + v\hat{\mathbf{e}}_y,\ p$ and T are the velocity, pressure and temperature respectively, and $\hat{\mathbf{e}}_x,\ \hat{\mathbf{e}}_y$ are the unit vectors in the x– and y–directions; the parameters Ra and Pr are the Rayleigh number and the Prandtl number, in turn, while $\Omega = [0,1] \times [0,8]$ denotes the dimensionless cavity.

The non-dimensional boundary conditions are:

$$\mathbf{u} = \mathbf{0} \quad \text{on } \partial\Omega, \tag{1.2a}$$

$$T = 0.5/-0.5 \quad \text{on left/right vertical walls } (x = 0/x = 1), \tag{1.2b}$$

$$\frac{\partial T}{\partial y} = 0 \quad \text{on horizontal walls } (y = 0, 8). \tag{1.2c}$$

To close the system, the initial conditions:

$$\mathbf{u} = \mathbf{u}_0 = \mathbf{0}, \quad T = T_0 = 0 \quad \text{in } \Omega \quad \text{at } t = 0 \tag{1.3a,b}$$

were chosen.

2 Numerical Approximation

2.1 Temporal Discretisation

In order to meet the demands of efficiency and accuracy, and avoid problems caused by numerical damping and/or over-smoothing, the time-discretisation procedure for the governing system requires judicious selection. The methods employed for the Navier–Stokes and energy equations are described in the following subsections.

2.1.1 Navier–Stokes part

Given the nature of the flow problem, i.e. advection-dominated, it was necessary to choose an appropriate method of time discretisation which could be both A-stable and non-dissipative, as well being inherently accurate (preferably, second-order).

The fractional θ–scheme with operator splitting as variant ([3], [1]) seemed therefore a suitable option, and in addition led to a favourable decoupling of the incompressibility constraint and the nonlinearity. The underlying mechanism of this procedure can perhaps best be observed by considering the following N–dimensional, first-order equation:

$$\frac{d\mathbf{q}}{dt} + A\mathbf{q} = \mathbf{0} \quad \text{for } t > 0, \tag{2.1a}$$

with initial condition

$$\mathbf{q}(0) = \mathbf{q}_0, \tag{2.1b}$$

where A is a known $N \times N$ matrix, $\mathbf{q}_0$ is a known N–vector, and, for $t > 0$, $\mathbf{q}(t)$ is an unknown N–vector to be determined. To solve (2.1a,b) computationally, we first break the integration step into three smaller sub-steps $[t_n, t_n + \theta\tau_n]$, $[t_n + \theta\tau_n, t_n + (1-\theta)\tau_n]$ and $[t_n + (1-\theta)\tau_n, t_{n+1}]$ with $\tau_n := t_{n+1} - t_n$ denoting the total timestep, and $\theta \in (0, 0.5)$ an arbitrary parameter. Then, for each interval, we 'split' the matrix-vector term into an implicit and an explicit part, with each part a non-trivial linear multiple of the original term evaluated at the 'current' and 'previous' time, respectively; this is performed in the following manner:

$$\frac{\mathbf{q}^{n+\theta} - \mathbf{q}^n}{\theta\tau_n} + \alpha A\mathbf{q}^{n+\theta} + (1-\alpha)A\mathbf{q}^n = \mathbf{0}, \tag{2.2a}$$

$$\frac{\mathbf{q}^{n+1-\theta} - \mathbf{q}^{n+\theta}}{(1-2\theta)\tau_n} + \alpha A\mathbf{q}^{n+\theta} + (1-\alpha)A\mathbf{q}^{n+1-\theta} = \mathbf{0}, \tag{2.2b}$$

$$\frac{\mathbf{q}^{n+1} - \mathbf{q}^{n+1-\theta}}{\theta\tau_n} + \alpha A\mathbf{q}^{n+1} + (1-\alpha)A\mathbf{q}^{n+1-\theta} = \mathbf{0}, \tag{2.2c}$$

where $\alpha \in (1/2, 1)$ is the single parameter controlling the splitting of the matrix-vector term.

With the choice $\theta = 1 - \sqrt{2}/2 (\approx 0.293)$, we obtain a second-order accurate method, which for *positive-definite* matrices A is unconditionally stable. Furthermore, choosing $\alpha = (1-2\theta)/(1-\theta) (\approx 0.586)$, ensures identical implicit operators for each of the three sub-intervals, which eases computation.

Another important advantage of the fractional θ–scheme is that eigenmodes are *uniformly* damped, allowing steady-state flows (or 'near- steady-state flows', as is relevant here) to be more reliably calculated.

In [3], the fractional θ–scheme was applied with operator splitting as variant to the Navier–Stokes equations $(1.1a, b, 1.2a, 1.3a)$ in the following manner:

$$\begin{aligned} \frac{\mathbf{u}^{n+\theta} - \mathbf{u}^n}{\theta\tau_n} - \alpha\sqrt{\frac{Pr}{Ra}}\Delta\mathbf{u}^{n+\theta} + \nabla p^{n+\theta} &= T^n\hat{\mathbf{e}}_y + (1-\alpha)\sqrt{\frac{Pr}{Ra}}\Delta\mathbf{u}^n \\ &\quad - (\mathbf{u}^n \cdot \nabla)\mathbf{u}^n \quad \text{in } \Omega, \\ \nabla \cdot \mathbf{u}^{n+\theta} &= 0 \quad \text{in } \Omega, \\ \mathbf{u}^{n+\theta} &= \mathbf{0} \quad \text{on } \delta\Omega; \end{aligned} \tag{2.3a-c}$$

$$\begin{aligned} \frac{\mathbf{u}^{n+1-\theta} - \mathbf{u}^{n+\theta}}{(1-2\theta)\tau_n} &+ (1-\alpha)\sqrt{\frac{Pr}{Ra}}\Delta\mathbf{u}^{n+1-\theta} + (\mathbf{u}^{n+1-\theta} \cdot \nabla)\mathbf{u}^{n+1-\theta} \\ &= T^n\hat{\mathbf{e}}_y + \alpha\sqrt{\frac{Pr}{Ra}}\Delta\mathbf{u}^{n+\theta} - \nabla p^{n+\theta} \quad \text{in } \Omega, \\ \mathbf{u}^{n+\theta} &= \mathbf{0} \quad \text{on } \delta\Omega; \end{aligned} \tag{2.4a-c}$$

$$
\begin{aligned}
\frac{\mathbf{u}^{n+1}-\mathbf{u}^{n+1-\theta}}{\theta\tau_n} - \alpha\sqrt{\frac{Pr}{Ra}}\Delta\mathbf{u}^{n+1} + \nabla p^{n+1} &= T^n\hat{\mathbf{e}}_y \\
&\quad + (1-\alpha)\sqrt{\frac{Pr}{Ra}}\Delta\mathbf{u}^{n+1-\theta} - (\mathbf{u}^{n+1-\theta}\cdot\nabla)\mathbf{u}^{n+1-\theta} \quad \text{in } \Omega, \\
\nabla\cdot\mathbf{u}^{n+1} &= 0 \quad \text{in } \Omega, \\
\mathbf{u}^{n+1} &= \mathbf{0} \quad \text{on } \delta\Omega;
\end{aligned}
\tag{2.5a-c}
$$

In the above we note that the nonlinear convection term is treated explicitly in the first and third steps, but implicitly in the second step; these rôles are exactly reversed for the pressure gradient, while the incompressibility constraint is relaxed in the second step. The general upshot of this form of discretisation is to produce two distinct types of sub-problem: (i) a self-adjoint, quasi-linear, Stokes system for unknown velocity and pressure; and (ii) an asymmetric, nonlinear system for velocity only. These subproblems are addressed in Section 3 below.

Finally, we note that the thermal source terms are approximated using the (explicit) temperature value at time t_n, for each of the three steps. This simple discretisation generally leads to the above scheme being only first-order accurate, but we apply this nonetheless, since the *overall* system (due to the 'first-order accuracy only' of the two types of energy-equation time discretisations considered – see below) is forced to have this degree of accuracy anyway.

2.1.2 Energy Equation

To assess and compare the effectiveness of different forms of time discretisation for the energy equation, we considered two possibilities: a first-order backward–Euler scheme and a Crank–Nicholson scheme, both with first-order velocity coupling.

(a) Backward–Euler/Semi–Implicit Advection (BE)

With τ_n defined as above, we determine T^{n+1}, for given T^n, $\mathbf{u}^n$, from:

$$
\frac{T^{n+1}-T^n}{\tau_n} + (\mathbf{u}^n\cdot\nabla)\,T^{n+1} - \frac{1}{\sqrt{RaPr}}\Delta T^{n+1} = 0. \tag{2.6}
$$

Here we note that the advection term is treated in a semi-implicit fashion, using the previous velocity value ($\mathbf{u}^n$) in its approximation. Although simple to implement and naturally stable (unconditionally, moreover), this scheme suffers from numerical dissipation, as well as being only first-order accurate – hence, not ideally suited to the nature of the problem in hand (as reflected to a certain extent in the results below).

(b) Crank–Nicholson/Semi–Implicit Advection (CN)

In this instance, our time-discretised equations adopt the form:

$$
\frac{T^{n+1}-T^n}{\tau_n} + (\mathbf{u}^n\cdot\nabla)\left(\frac{T^{n+1}+T^n}{2}\right) - \frac{1}{\sqrt{RaPr}}\Delta\left(\frac{T^{n+1}+T^n}{2}\right) = 0. \tag{2.7}
$$

As in (a), the velocity part of the advection term is treated explicitly, making the scheme first-order overall. An important distinction however is the inherent property of non-dissipativeness associated with Crank–Nicholson-type schemes.

We note that both schemes lead to asymmetric systems, whose solution procedure will be described in Subsection 3.2 below.

2.2 Finite–Element Discretisation

For the spatial discretisation of the governing equations $(1.1-1.3)$, a standard Bubnov–Galerkin finite-element method was applied using continuous, piecewise bi-quadratic basis functions for the discrete velocity and temperature spaces ($:= V_h$), and continuous, piecewise bilinear basis functions for the discrete pressure space ($:= W_h$), i.e. the Taylor–Hood element. This element, fulfilling the requirements of the inf–sup (LBB) stability constraint, avoids any possible complications with spurious pressure modes, and, as well as being relatively straightforward to implement, gives a good balance between efficiency of computation and accuracy. For this element, the velocity and temperature are of second-order spatial accuracy, while pressure is of first-order spatial accuracy.

2.3 Computational Procedure

Before describing the solution methods for the two subproblems stemming from the time discretisation, we first recapitulate the main aspects of the numerical solution procedure, in order of application:

(a) Specify $\mathbf{u}_0, T_0$. (Both are zero-valued here.)

For $n \geq 0$:

(b) Solve the energy equation for $t_n \rightarrow t_{n+1}$.

(c) Solve the Navier–Stokes equations with incompressibility constraint for:

(i) $t_n \rightarrow t_{n+\theta}$,

(ii) $t_{n+\theta} \rightarrow t_{n+1-\theta}$,

(iii) $t_{n+1-\theta} \rightarrow t_{n+1}$.

(d) Repeat (b),(c) until end-time = t_E.

3 Algebraic Subproblems

3.1 Quasi–Steady Stokes System

As demonstrated in the previous section, the application of the fractional θ–scheme to the Navier–Stokes part of our model equations renders a linear, self-adjoint system for the first and third substeps, these resembling the steady Stokes equations. After full (time and space) discretisation, we need to solve a matrix system of the form:

$$\begin{pmatrix} A(\gamma_n) & B \\ B^T & 0 \end{pmatrix} \begin{pmatrix} u_h^c \\ p_h^c \end{pmatrix} = \begin{pmatrix} f_h^c \\ 0 \end{pmatrix}. \tag{3.1}$$

Here $A(\gamma_n)$ is the symmetric, positive-definite (SPD) stiffness matrix for the discrete velocity $\mathbf{u}_h = (u_h, v_h)$ whose corresponding coordinate vector (with respect to the given basis functions of the discrete velocity space, V_h) is $u_h^c = \left[u_h^1, \cdots, u_h^{N_v} | v_h^1, \cdots, v_h^{N_v}\right]$, with N_v denoting the dimension of V_h, i.e. the number of velocity 'nodes'. The matrix A depends on the discretisation parameter $\gamma_n := \theta \tau_n \alpha \sqrt{Pr/Ra}$, which we note is small in the problem under observation, (e.g. $\gamma_n = 2.48 \times 10^{-5}$ for a time-step as large as 0.1). Also in (3.1), we have the discrete gradient matrix B, its transpose (which represents discrete divergence), and the pressure vector, which has an analogous definition to that for velocity, i.e. $p_h^c = \left[p_h^1, \cdots, p_h^{N_p}\right]$, with N_p the number of pressure 'nodes'. Finally f_h^c denotes the coordinate vector of the discrete momentum source term f_h. For brevity, we have dispensed with the timestep superscripts on the vector quantities.

Since A is invertible, we can form the Schur complement equation for the pressure vector as follows:

$$C(\gamma_n) p_h^c := \left(B^T A^{-1}(\gamma_n) B\right) p_h^c = A^{-1} f_h^c. \tag{3.2}$$

Moreover, since B has full rank and, owing to the relatively small pressure space ($\dim W_h < \dim V_h$) for the Taylor–Hood element, has more rows than columns, it follows that C is SPD for any given (positive) γ_n. Unfortunately, however, its condition number explodes as $\gamma_n \to 0^+$, precluding the possibility of applying a suitable minimisation solver, such as the method of conjugated gradients (CG method). To circumvent the problem of large condition number, we apply a special type of preconditioner, as first proposed in [3]. For the spatially-continuous analogue of the problem here, this amounts to applying the operator S given by:

$$Sq := \gamma_n q + \phi_q, \tag{3.3}$$

where $S : L_2(\Omega)/R \to L_2(\Omega)/R$,

$$q = -\nabla \cdot \mathbf{u}, \tag{3.4}$$

and ϕ_q is the unique solution of:

$$\begin{aligned} -\Delta \phi_q &= q \quad \text{in } \Omega, \\ \frac{\partial \phi_q}{\partial n} &= 0 \quad \text{on } \partial\Omega, \\ \int_\Omega \phi_q d\Omega &= 0. \end{aligned} \tag{3.5a-c}$$

We can similarly define a preconditioner in our discrete problem, i.e. $S_h : W_h \to W_h$, with analogous properties; the only fundamental modification required is in the definition of q_h, the discrete version of q, since, in general, $\nabla \cdot \mathbf{u}_h \notin W_h$. To this end, we define q_h to be the *projection* of $(-\mathbf{u}_h)$ onto W_h, i.e. q_h satisfies:

$$(q_h; \psi_i) = -(\nabla \cdot \mathbf{u}_h; \psi_i), \tag{3.6}$$

for $i = 1, \cdots, N_p$, where $(\cdot;\cdot)$ denotes the $L_2(\Omega)$ inner product.

Utilising the above preconditioner leads to three matrix systems, all involving SPD matrices, and all solved by the CG method: firstly, for fixed pressure, we solve for velocity, via the momentum equation

$$A(\gamma_n)u_h^c = f_h^c - Bp_h^c; \tag{3.7}$$

secondly, the pressure projection system (3.6) is solved; finally, the updated pressure value is obtained after solving the discrete form of the Poisson problem (3.5a-c). If the velocity is not discretely 'divergence-free' (in practice, smaller than a given tolerance value), then this pressure value is substituted into (3.7) and the cycle is repeated continuously until the 'divergence-free' criterion is fulfilled.

3.2 Asymmetric Advection System

This system, which arises from the spatially-discretised form of the second step of the fractional θ–scheme for the Navier–Stokes equations, as well as from the full discretisation of the energy equation, has the general form:

$$Mx_h^c = g_h^c, \tag{3.8}$$

where M is an *asymmetric* $2N_v \times 2N_v$ (or $N_v \times N_v$, as appropriate) stiffness matrix for the coefficient vector $x_h^c = \left[u_h^1, \cdots, u_h^{N_v} | v_h^1, \cdots, v_h^{N_v}\right]$ $\left(\text{or } \left[T_h^1, \cdots, T_h^{N_v}\right]\right)$, and g_h^c the source term. Furthermore, we note that M is variable dependent, in the former case. To solve this matrix system, we applied the GMRES solver [6] using a Krylov subspace dimension of 15. In addition, for the velocity solver, the 'current' velocity value was periodically used to update the matrix M.

4 Grid Generation

Following the guidelines suggested in the Special Session Document [2], we selected grids aligned with the coordinate directions and composed of E_x elements in the x–direction and E_y elements in the y–direction with $E_x : E_y \approx 1:5 \quad (\to 1:5, \text{ as } E_x,\ E_y \to \infty.)$ Specifically, we ran our computations on three different grids with increasing refinement: 11×51 elements ('coarse'), 21×101 elements ('medium') and 41×201 elements ('fine').

Owing to the rapid flow-variable changes near the walls, in particular the presence of strong thermal boundary layers on the vertical walls (see Figure 1, for example), the grid required appropriate grading in these regions. For this purpose, we defined the following functions:

$$h_1(j) = \left(\frac{\hat{h}_1(j)}{\sum_{j_1=1}^{E_x} \hat{h}_1(j_1)} \right) W, \qquad \text{for } j = 1, \cdots, E_x, \tag{4.1a}$$

$$h_2(k) = \left(\frac{\hat{h}_2(k)}{\sum_{k_1=1}^{E_y} \hat{h}_2(k_1)} \right) H, \qquad \text{for } k = 1, \cdots, E_y. \tag{4.1b}$$

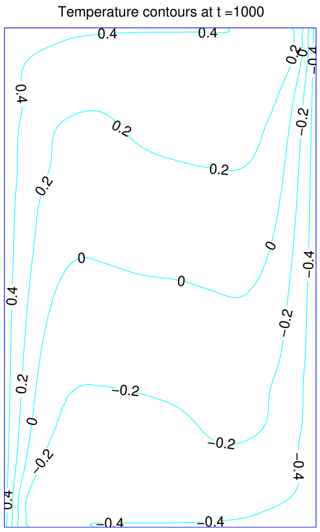

Figure 1: Temperature contours for non-dimensional time $t = 1000$

These functions determine the width of the jth element in the horizontal direction, and the length of the kth element in the vertical direction, respectively, where $W(=1)$ denotes cavity width and $H(=8)$ cavity height.

Here

$$\hat{h}_1(j) = \frac{1}{\bar{h}_1(E_x+1-2j)^2+2}, \qquad \text{for } j = 1, \cdots, E_x, \tag{4.2a}$$

and

$$\hat{h}_2(k) = \frac{1}{\bar{h}_2|E_y+1-2k|+2}, \qquad \text{for } k = 1, \cdots, E_y, \tag{4.2b}$$

control the element width and length distributions, respectively, for given E_x, E_y, where:

$$\bar{h}_1 := W/E_x, \quad \bar{h}_2 := H/E_y, \tag{4.3a,b}$$

are the average element width and average element height, in turn.

In Figure 2a a graded grid of medium refinement is displayed, revealing, in particular,the relative fineness at the walls; this is shown in greater detail for the south-west corner of the cavity in Figure 2b, where the minimal element size is 0.012×0.04. This region of the cavity, together with its north-east counterpart (due to skew symmetry), was found to be the most sensitive location in general, as regards rapid physical flow changes within the cavity. This is evidenced, for example, by the strong thermal boundary layers of Figure 1 (allowing for the five-fold vertical compression); indeed, we based our verification that the grids were sufficiently graded near the walls, on whether or not the temperature profile was sufficiently 'smooth' near the horizontal and vertical walls. All three grid types (coarse, medium and fine) were adjudged to pass this 'test' for the given grid functions defined in (4.1). Furthermore, with simple real analysis it can be shown that *near the horizontal and vertical walls*:

$$h_1 \sim \left(\frac{2\sqrt{2W}}{\pi}\right) E_x^{-3/2}, \quad h_2 \sim \left(\frac{H^2}{(H+2)\log(1+H/2)}\right) E_y^{-1}, \tag{4.4a,b}$$

as $E_x \to \infty, E_y \to \infty$, respectively.

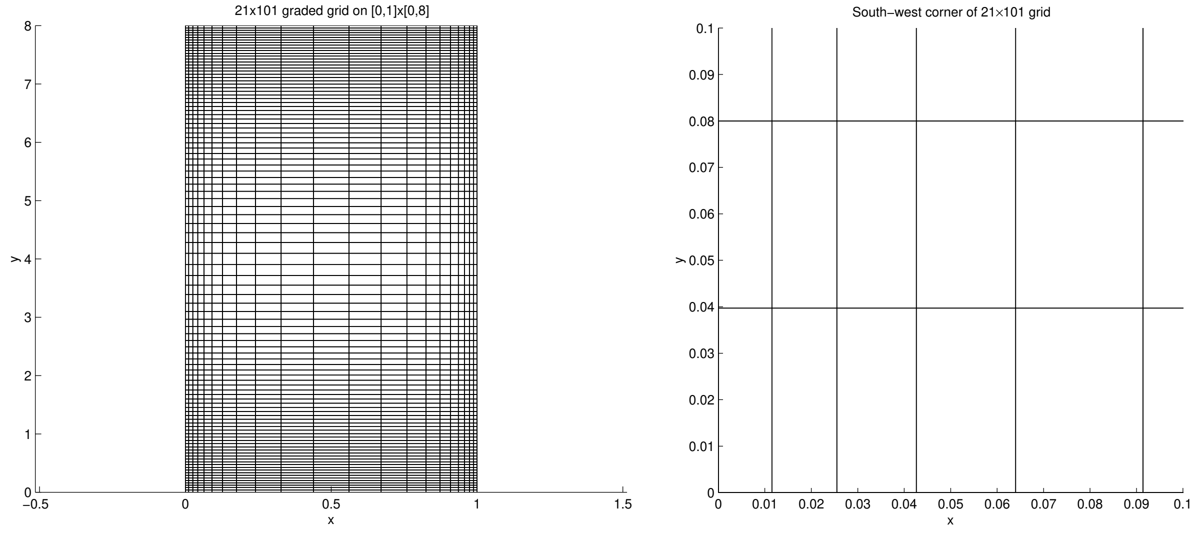

(a) (b)

Figure 2: Graded grid of a medium level of refinement; (a) the whole domain; (b) a close-up of the south-west corner.

5 Results

Computational results were obtained for each of the three grid types, and for both types of energy solver – hence, a total of six cases. Based on the time history of the flow solution at various 'points' in the cavity (see Table 1), the computations reveal an initial 'active' transient state lasting approximately 500 non-dimensional time units preceding a single-frequency periodic state, as illustrated, for example, by Figure 3. Here the temperature and velocity components in point 1, and the pressure difference between points 1 and 4 are shown. These same flow quantities are then depicted over a number of periods in Figure 4.

Point	x–coordinate	y–coordinate
1	0.1810	7.3700
2	0.8190	0.6300
3	0.1810	0.6300
4	0.8190	7.3700
5	0.1810	4.0000

Table 1: Point locations in cavity

Three different forms of data were required for the benchmark test, the first of these being 'point data', based on the measurement of flow quantities at the given points in the cavity. The measurement here is based on the average, amplitude (half peak-to-valley) and the period of the flow quantity under scrutiny. Before recording measurements however, the period and amplitude per cycle were first checked for consistency over ten cycles, to ensure that the flow was truly periodic. To calculate the average of the flow quantity we used Matlab's internal function. Tables 2 and 3 show point data for the energy-equation solvers BE and CN. An immediate observation from the tables is that both solvers fail to produce oscilla-

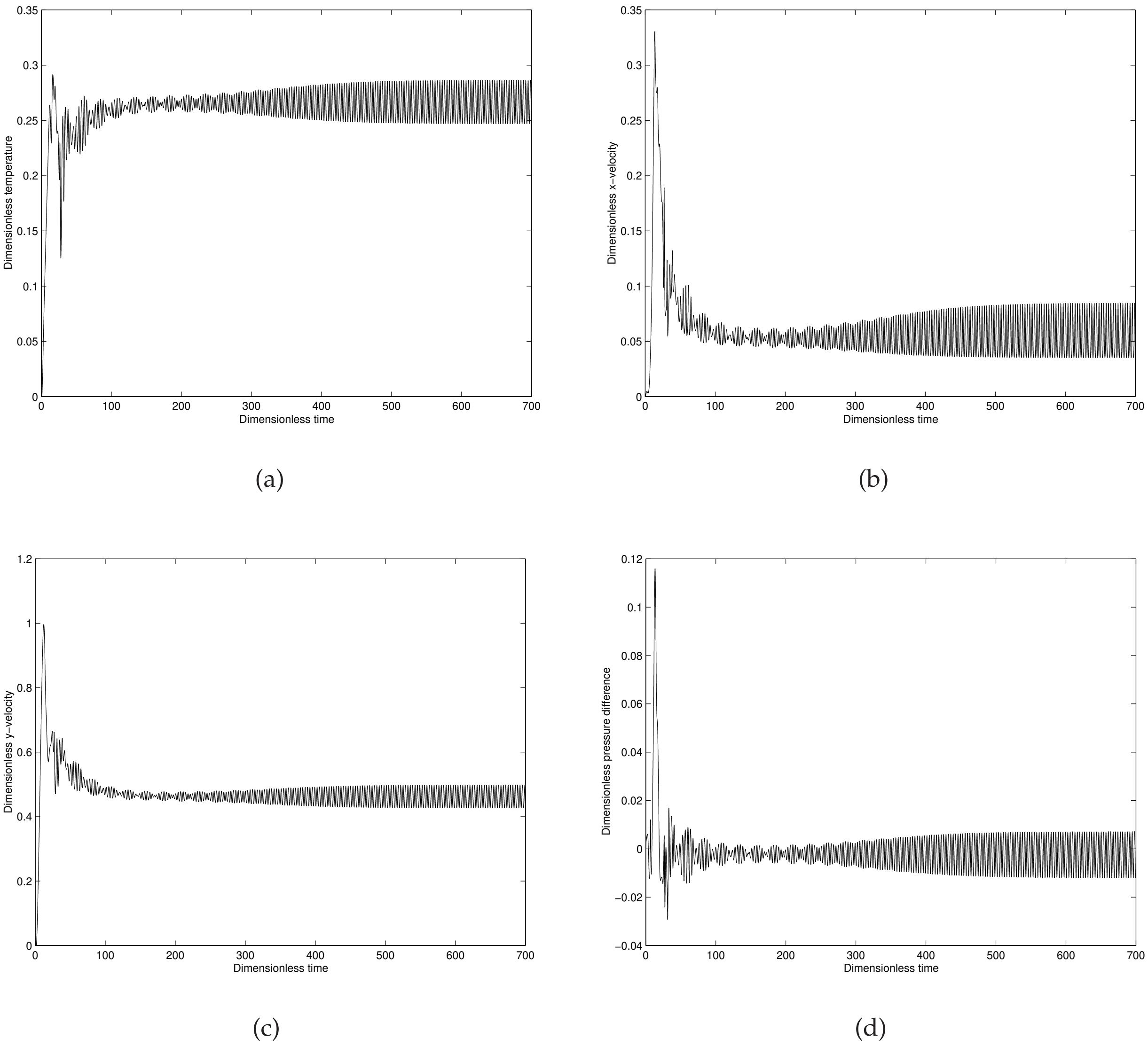

Figure 3: Time histories of dimensionless flow quantities; (a) temperature in point 1; (b) x–velocity component in point 1; (c) y–velocity component in point 1; (d) pressure difference between points 1 and 4.

tory motion for the coarse grid case – this merely confirms one of the known disadvantages of working with the Taylor–Hood $Q_2 - Q_1$ element, i.e. its inaccuracy on coarse grids (see [4],pp 750–767 for a comparison of accuracy between various quadrilateral finite elements). The averages of the flow quantities can be seen to be most consistent, while the amplitudes are the least consistent; there is also a discrepancy between the values for the amplitudes obtained for the BE and CN cases – our belief however (given the theoretical knowledge on the types of solver) is that this is principally due to the numerical damping effects present in the former case, and therefore we put more faith in our calculated amplitudes for CN (which theoretically has no numerical dissipative effects) – this was later confirmed by the accepted 'true' numerical values from [8]. Other noticeable features include the negligible skewness (defined as the average of the temperature values at points 1 and 2) found in all cases, and implying the expected antisymmetric nature of the perturbation. Finally, we can see that the calculated period differs only slightly from the medium grid to the fine grid; our 'best' prediction of this was 3.412, (based on the fine grid of CN), and this turned out to have a deviation of just 0.015% from the 'true' solution of [8].

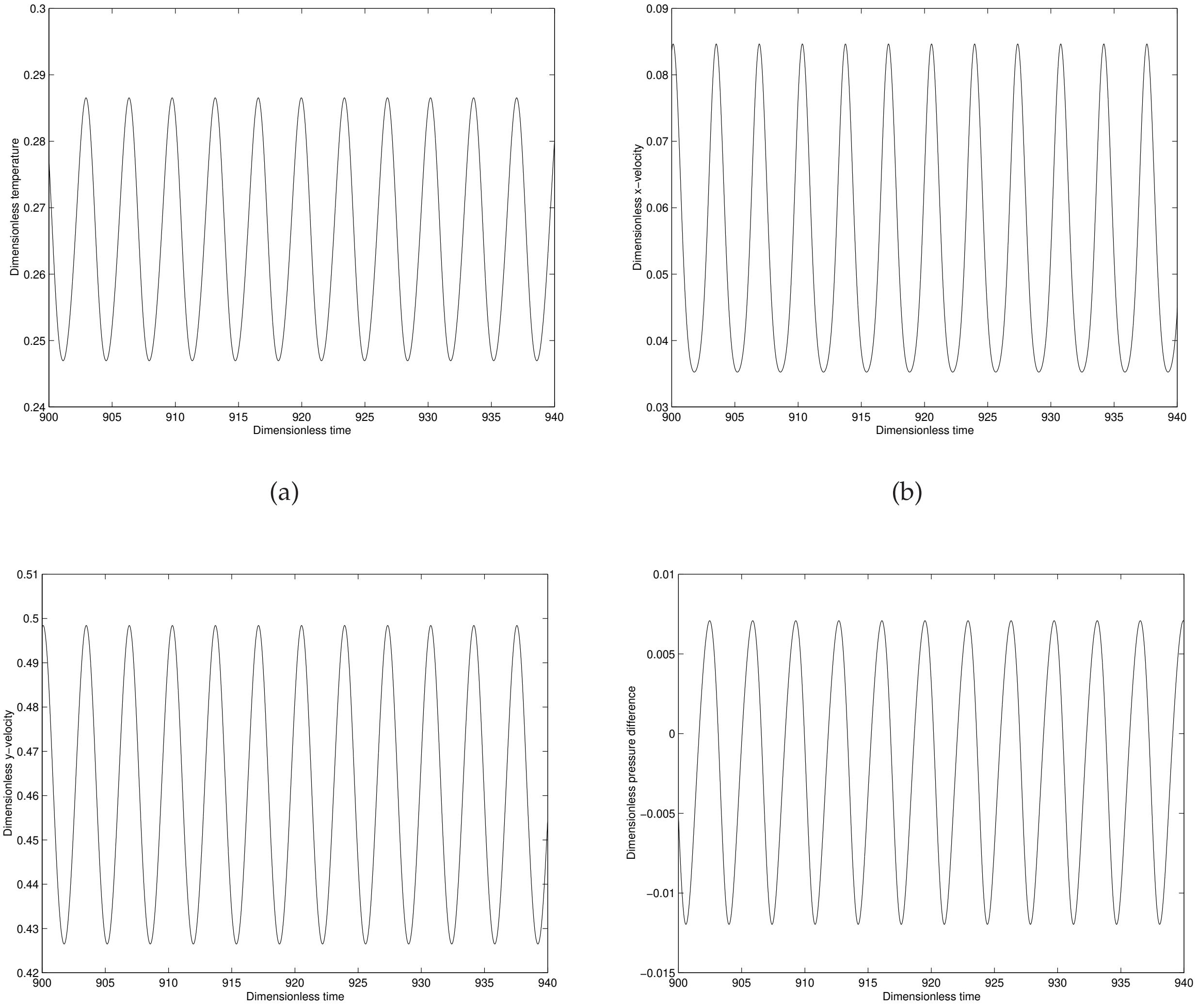

(a) (b)

(c) (d)

Figure 4: Oscillatory behaviour of flow quantities during periodic phase; (a) temperature in point 1; (b) x–velocity component in point 1; (c) y–velocity component in point 1; (d) pressure difference between points 1 and 4.

Next, 'wall data' values were recorded, specifically, the Nusselt numbers on the vertical walls,

$$Nu(t) := \frac{1}{H} \int_0^H \left(\frac{\partial \theta}{\partial x} \right)_{x=0,W} dy. \tag{5.1}$$

We firstly note that the anti-symmetry of the flow perturbation should ensure that the values are identical on each wall – this proved to be the case. Figure 5 shows the time history dependence of the Nusselt number on either vertical wall, and reveals very strong initial wall gradients becoming heavily damped before the periodic phase is reached. This again underlines the need for careful grading on the walls, especially during the initial stages of the transient phase. Table 4 shows the Nusselt values for the CN solver, and for the non-stationary cases (medium and fine grids) we see that the average has a value around -4.58, while the amplitude is relatively small at $O(10^{-3})$.

Finally, 'global data' in the form of a velocity metric, defined as the square root of the kinetic energy (KE),

$$\hat{u}(t) := \sqrt{\frac{1}{2A_c}\int_\Omega \mathbf{u}\cdot\mathbf{u}\,d\Omega}, \tag{5.2}$$

was computed, where A_c is the area of the cavity, i.e. $A_c = W \times H (= 8)$. Figure 6a shows the time history of the velocity metric from a global perspective, and it can be seen that this quantity appears to approach steady state, as the periodic phase is approached. In fact, closer

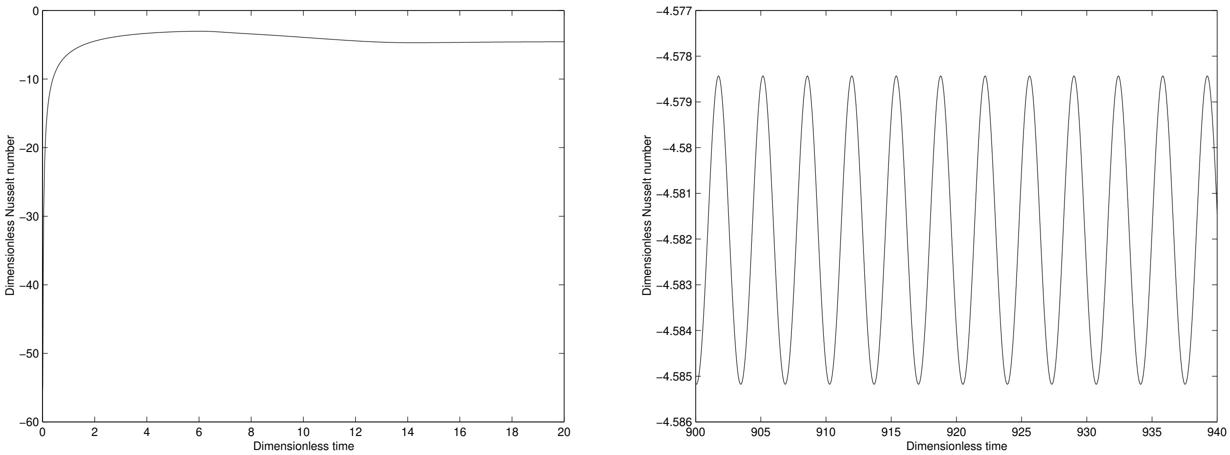

(a) (b)

Figure 5: Time history of the Nusselt number on vertical walls: (a) global profile; (b) local oscillatory behaviour during periodic phase.

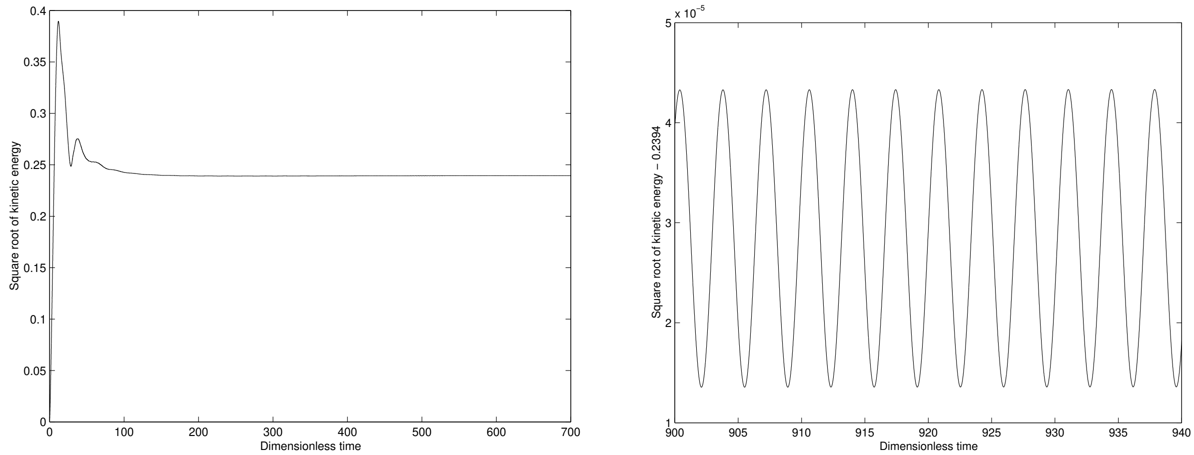

(a) (b)

Figure 6: Time history of the velocity metric ($= \sqrt{\mathrm{KE}}$): (a) global profile; (b) local oscillatory behaviour during periodic phase (zeroed on 0.2394).

inspection (Figure 6b) reveals that the velocity metric undergoes small periodic oscillations during this phase. This behaviour is attributable to a weak viscous dissipation ($\sim (Pr/Ra)^{1/2}$) of the rate of change of KE, as can be verified directly by taking the $L_2(\Omega)$ inner product of the momentum terms and the velocity and implementing the incompressibility condition and the homogeneous velocity boundary conditions. In Table 5 the specific velocity metric values are tabulated and they indicate that a characteristic value for the speed of fluid in the whole domain is about 0.240.

	Grid resolution:11x51 Time duration: N/A Steps per period: N/A			Grid resolution:21x101 Time duration: 50 Steps per period: 344			Grid resolution:41x201 Time duration: 50 Steps per period: 344		
Quantity	Ave	Amp	Per	Ave	Amp	Per	Ave	Amp	Per
X–velocity	0.055	S	S	0.058	0.023	3.44	0.056	0.023	3.44
Y–velocity	0.463	T	T	0.461	0.034	3.44	0.462	0.034	3.44
Temperature	0.264	E	A	0.266	0.018	3.44	0.266	0.018	3.44
Skewness	0	A	T	0	–	–	0	–	–
ΔP_{14}	-0.001	D	E	-0.002	0.009	3.44	-0.002	0.009	3.44
ΔP_{51}	-0.528	Y		-0.534	0.010	3.44	-0.535	0.010	3.44
ΔP_{35}	0.529			0.536	0.004	3.43	0.537	0.004	3.44

Table 2: Point data computed using the BE solver

	Grid resolution:11x51 Time duration: N/A Steps per period: N/A			Grid resolution:21x101 Time duration: 50 Steps per period: 341			Grid resolution:41x201 Time duration: 50 Steps per period: 341		
Quantity	Ave	Amp	Per	Ave	Amp	Per	Ave	Amp	Per
X–velocity	0.0551	S	S	0.0552	0.0247	3.408	0.0563	0.0271	3.412
Y–velocity	0.4632	T	T	0.4613	0.0360	3.407	0.4617	0.0382	3.413
Temperature	0.2641	E	A	0.2655	0.0198	3.407	0.2655	0.0211	3.412
Skewness	0	A	T	0	–	–	0	–	–
ΔP_{14}	-0.0014	D	E	-0.0021	0.0096	3.407	-0.0018	0.0101	3.412
ΔP_{51}	-0.5279	Y		-0.5343	0.0106	3.409	-0.5347	0.0111	3.413
ΔP_{35}	0.5293			0.5362	0.0046	3.407	0.5366	0.0050	3.412

Table 3: Point data computed using the CN solver

Quantity	Grid resolution:11x51 Time duration: N/A Steps per period: N/A Ave	Amp	Per	Grid resolution:21x101 Time duration: 50 Steps per period: 341 Ave	Amp	Per	Grid resolution:41x201 Time duration: 50 Steps per period: 341 Ave	Amp	Per
Nu ($x = 0$)	-4.6217	ST.	ST.	-4.5819	0.0034	3.408	-4.5796	0.0035	3.412
Nu ($x = W$)	-4.6217	STATE	STATE	-4.5819	0.0034	3.408	-4.5796	0.0035	3.412

Table 4: Wall data computed using the CN solver

Quantity	Grid resolution:11x51 Time duration: N/A Steps per period: N/A Ave	Amp	Per	Grid resolution:21x101 Time duration: 50 Steps per period: 341 Ave	Amp	Per	Grid resolution:41x201 Time duration: 50 Steps per period: 341 Ave	Amp	Per
$\hat{u}$ ($= \sqrt{\mathrm{KE}}$)	0.2400	ST.	STATE	0.2394	1.49×10^{-5}	3.407	0.2395	1.65×10^{-5}	3.412

Table 5: Global data computed using the CN solver

6 Benchmark Performance Metrics

In order to assess the comparative performances of the 30 contributions to the benchmark test, a number of metrics based on the quantities shown in Tables 2–5 were defined; the values obtained by each participant were compared against the accepted values of [8], and the deviations from these latter values defined the metrics; hence, values as close to zero as possible were the 'target', whilst large metrics indicated high 'error'. A full transcript of these performance metrics can be downloaded from http://wotan.me.unm.edu/˜christon/mit_convection/summary/. Here we just summarise our own performance, based on the six "overall basis" metrics, namely:

(a) Average of the mean differences in Nu, u_1, T_1:

$$M_1 := \frac{(\bar{\varepsilon}_{Nu} + \bar{\varepsilon}_{u_1} + \bar{\varepsilon}_{T_1})}{3} \tag{6.1}$$

(b) Average of amplitude/period ($:= \tau$) differences:

$$M_2 := \frac{(\varepsilon_{\tau_{T_1}} + \varepsilon'_{Nu} + \varepsilon'_{T_1} + \varepsilon'_{u_1})}{4} \tag{6.2}$$

(c) Average of mean, amplitude and period:

$$M_3 := \frac{(\bar{\varepsilon}_{Nu} + \bar{\varepsilon}_{u_1} + \bar{\varepsilon}_{T_1} + \bar{\varepsilon}_{\tau_{T_1}} + \varepsilon'_{Nu} + \varepsilon'_{T_1} + \varepsilon'_{u_1})}{7} \tag{6.3}$$

(d) Metric in (c) weighted by grid resolution:

$$M_4 := M_3 \cdot (\text{\# of nodes}) \tag{6.4}$$

(e) Metric in (c) weighted by algorithm timing:

$$M_5 := M_3 \cdot \left[\frac{\text{CPU}}{\text{grid pt}\cdot\text{timestep}} \cdot \frac{\text{timestep}}{\text{period}}\right] \cdot \text{specFP95} \tag{6.5}$$

(f) Metric in (c) weighted by resolution and timing:

$$M_6 := M_3 \cdot (\text{\# of nodes}) \cdot \left[\frac{\text{CPU}}{\text{grid pt}\cdot\text{timestep}} \cdot \frac{\text{timestep}}{\text{period}}\right] \cdot \text{specFP95} \tag{6.6}$$

Here $\bar{\varepsilon}_q$, ε'_q and ε_q denote the deviations in mean, amplitude and period of the given subscripted flow quantity q, respectively. A summary of our performance using these metrics is given in Table 6.

Metric	Value	Mean	Standard Deviation	Ranking
M_1	0.0367%	2.8557%	6.2259%	2 (/30)
M_2	0.9580%	14.6549%	19.0872%	2 (/30)
M_3	0.5631%	9.6143%	13.0837%	2 (/30)
M_4	9.017	169.997	228.758	5 (/28)
M_5	144.04	2034.19	7888.57	12 (/24)
M_6	574.62	3301.16	7783.79	12 (/24)

Table 6: Performance metrics

7 Computational Resources

The computations were performed on a Compaq XP1000 (single processor) machine with a clock rate of 500MHz, total memory of 256MB, a peak flop of 500MFLOPs and a Specfp95 rating of 53.9. The CPU/grid point/time step was measured to be approximately 490μs/pt. /step, while approximately 4KB of memory per grid point was required.

8 Conclusions

The computational results (as reflected, to a degree, in Tables 2 and 3) suggest that the amplitudes of the flow quantities are the most sensitive to timestep size and grid resolution, compared to the averages and the periods. Despite this however, a timestep size of 0.01 on the finest grid (41×201 elements) proved to be sufficient in obtaining a (timestep- and grid-) converged and (based on the benchmark metrics 1–4 of Table 6) accurate solution.

In general, the CN solver performed better (regarding accuracy) than the BE solver (and at no extra cost in terms of computing time), and in view of the earlier comments on numerical damping with advection-dominated problems, this is perhaps no surprise. However, both solvers failed to yield a periodic solution after the transient phase on the coarsest grid (11×51 elements), although this is probably attributable to the intrinsic inaccuracy of the $Q_2 - Q_1$ finite element on 'too-coarse' grids. (By comparison, the elements $Q_1 - Q_0$ (bilinear velocity and temperature, piecewise-constant pressure) and $Q_2 - Q_{-1}$ (biquadratic velocity and temperature, piecewise-bilinear pressure) were reported to yield periodic solutions on a grid of comparable coarseness to our 'coarse' version [5], although it should also be noted that these elements fail the inf–sup stability condition. The accuracy of the $Q_2 - Q_1$ element on sufficiently fine grids was also reported by another benchmark contributor [7].)

Finally, we remark that we obtained virtually zero skewness in our calculations, a feature consistent with the anti-symmetric nature of the instability mode [2].

References

[1] Bänsch, E. Simulation of instationary, incompressible flows. *Acta Math. Univ. Comenianae*, LXVII:101–114, 1998.

[2] Christon, MA, Gresho, PM and Steven B. Sutton. Computational predictability of natural convection flows in enclosures. In *Computational Fluid and Solid Mechanics, Boston, Massachusetts, June 12–15, 2001*, volume 2, 2001.

[3] Bristeau, MO, Glowinski, R and Periaux, J. Numerical methods for the navier-stokes equations. applications to the simulation of compressible and incompressible flows. *Computer Physics Report*, 6:73–188, 2001.

[4] Gresho, PM and Sani, RL. *Incompressible flow and the finite element method. Vol. 2: Isothermal laminar flow*. John Wiley and Sons, Chichester, 2000.

[5] Gresho, PM and Sutton, SB. 8:1 thermal cavity problem. In *Computational Fluid and Solid Mechanics, Boston, Massachusetts, June 12–15, 2001*, volume 2, 2001.

[6] Saad, Y and Schultz, MH. GMRES: A generalised minimal residual algorithm for solving nonsymmetric linear systems. *Siam J. Sci. Stat. Comput.*, 7(3):856–869, 1986.

[7] Westerberg, KW. Thermally driven flow in a cavity using the Galerkin finite element method. In *Computational Fluid and Solid Mechanics, Boston, Massachusetts, June 12–15, 2001*, volume 2, 2001.

[8] Xin, S and le Quéré, P. An extended chebyshev pseudo-spectral contribution to the cpncfe benchmark. In *Computational Fluid and Solid Mechanics, Boston, Massachusetts, June 12–15, 2001*, volume 2, 2001.